

# Central concentration of warm and dense molecular gas in a strongly lensed submillimeter galaxy at $z=6$

Akiyoshi TSUJITA<sup>1</sup>, Ken-ichi TADAKI,<sup>2,3</sup> Kotaro KOHNO<sup>1,4</sup>, Bunyo HATSUKADE<sup>1</sup>, Fumi EGUSA<sup>1</sup>, Yoichi TAMURA<sup>5</sup>, Yuri NISHIMURA<sup>1</sup>, Jorge ZAVALA<sup>2</sup>, Toshiki SAITO<sup>2,6</sup>, Hideki UMEHATA<sup>7,5</sup> and Minju M. LEE<sup>8,9</sup>

<sup>1</sup>Institute of Astronomy, Graduate School of Science, The University of Tokyo, 2-21-1 Osawa, Mitaka, Tokyo 181-0015, Japan

<sup>2</sup>National Astronomical Observatory of Japan, 2-21-1 Osawa, Mitaka, Tokyo 181-8588, Japan

<sup>3</sup>Department of Astronomical Science, SOKENDAI (The Graduate University for Advanced Studies), Mitaka, Tokyo 181-8588, Japan

<sup>4</sup>Research Center for the Early Universe, Graduate School of Science, The University of Tokyo, 7-3-1 Hongo, Bunkyo-ku, Tokyo 113-0033, Japan

<sup>5</sup>Department of Physics, Graduate School of Science, Nagoya University, Furocho, Chikusa, Nagoya 464-8602, Japan

<sup>6</sup>Department of Physics, General Studies, College of Engineering, Nihon University, 1 Nakagawara, Tokusada, Tamuramachi, Koriyama, Fukushima 963-8642, Japan

<sup>7</sup>Institute for Advanced Research, Nagoya University, Furocho, Chikusa, Nagoya 464-8602, Japan

<sup>8</sup>Cosmic Dawn Center (DAWN), Jagtvej 128, DK-2200 Copenhagen N, Denmark

<sup>9</sup>DTU-Space, Technical University of Denmark, Elektrovej 327, DK2800 Kgs. Lyngby, Denmark

\*E-mail: tsujita@ioa.s.u-tokyo.ac.jp

Received ; Accepted

## Abstract

We report the detection of the CO(12-11) line emission toward G09-83808 (or H-ATLAS J090045.4+004125), a strongly-lensed submillimeter galaxy at  $z = 6.02$ , with Atacama Large Millimeter/submillimeter Array observations. Combining previously detected [O III]  $88 \mu\text{m}$ , [N II]  $205 \mu\text{m}$ , and dust continuum at 0.6 mm and 1.5 mm, we investigate the physical properties of the multi-phase interstellar medium in G09-83808. A source-plane reconstruction reveals that the region of the CO(12-11) emission is compact ( $R_{e,\text{CO}} = 0.49^{+0.29}_{-0.19}$  kpc) and roughly coincides with that of the dust continuum. Non-local thermodynamic equilibrium radiative transfer modeling of CO spectral-line energy distribution reveals that most of the CO(12-11) emission comes from a warm (kinetic temperature of  $T_{\text{kin}} = 320 \pm 170$  K) and dense ( $\log(n_{\text{H}_2}/\text{cm}^{-3}) = 5.4 \pm 0.6$ ) gas, indicating that the warm and dense molecular gas is concentrated in the central 0.5-kpc region. The luminosity ratio in G09-83808 is estimated to be  $L_{\text{CO}(12-11)}/L_{\text{CO}(6-5)} = 1.1 \pm 0.2$ . The high ratio is consistent with those in local active galactic nuclei (AGNs) and  $6 < z < 7$  quasars, the fact of which implies that G09-83808 would be a good target to explore dust-obscured AGNs in the epoch of reionization. In the reconstructed [O III]  $88 \mu\text{m}$  and [N II]  $205 \mu\text{m}$  cubes, we also find that a monotonic velocity gradient is extending

over the central starburst region by a factor of two and that star-forming sub-components exist. High-resolution observations of bright [C II]  $158\ \mu\text{m}$  line emissions will enable us to characterize the kinematics of a possible rotating disk and the nature of the sub-components.

**Key words:** galaxies: high-redshift — galaxies: starburst — galaxies: kinematics and dynamics

---

## 1 Introduction

In the current widely accepted scenario of the galaxy evolution, the submillimeter bright galaxy (SMG) evolves to a massive quiescent galaxy through the central starburst with the star formation rate of hundreds of  $M_{\odot}\text{yr}^{-1}$  caused by a major merger or gravitational disk instability. Recently, massive quiescent galaxies have been found at  $z \sim 4$ , suggesting that these galaxies experienced a starburst at the earlier epoch, which is estimated to be at  $z \gtrsim 5$  (e.g., Glazebrook et al. 2017).

A key to understanding how these early massive quiescent galaxies are formed is the physical property of the multi-phase interstellar medium (ISM) at the early epoch. One way to study it is to characterize the CO spectral-line energy distribution (CO SLED), which enables us to estimate the average physical properties of the molecular gas, such as kinetic temperature, molecular density, and gas mass. In particular, high- $J$  ( $J_{\text{up}} \geq 10$ ) CO lines trace warm and dense molecular gas with an upper energy level of  $E_{\text{up}} > 300\text{K}$  and a critical density of  $n_{\text{crit}} \sim 10^{5-8}\text{cm}^{-3}$ . Since the amount of globally integrated emission from high- $J$  CO lines is difficult to explain solely with star formation, a CO SLED containing bright high- $J$  lines provides information on the contribution of other high-energy heating mechanisms, such as an AGN, shock, and cosmic rays (e.g., Mashian et al. 2015).

For local objects at  $z \sim 0$ , high- $J$  ( $J_{\text{up}} \geq 10$ ) CO lines have been observed mainly with the *Herschel Space Observatory* or the Stratospheric Observatory for Infrared Astronomy because the lines are not observable from the ground. A major problem in such space observations is the difficulty in spatially resolving the targets due to the limited beam size of the instruments. Indeed, even the nearest ultraluminous infrared galaxy (ULIRG) practically appears, with *Herschel* observations, as a point source (Arp 220; Rangwala et al. 2011) because the beam size of its Spectral and Photometric Imaging Receiver ranges between a full width at half maximum of  $\approx 17''\text{--}43''$ . In contrast, for high- $z$  objects, high- $J$  CO lines are redshifted to a millimeter band and hence are observable with ground-based interferometers like ALMA. Ground-based observations allow us to study highly-excited molecular gas in distant galaxies with large collecting areas, sensitive receivers, and high angular resolution.

Tadaki et al. (2022) (hereafter referred to as ‘‘Paper I’’) concluded on the basis of the compact size of the dust-emission area and the high infrared surface brightness that G09-83808, a strongly-lensed ( $\mu \sim 8.4$ ) SMG at  $z = 6.02$ , is likely to be a progenitor of a massive quiescent galaxy at  $z \sim 4$ . This source has a flux density of  $S_{870,\text{intr}} \sim 4\text{mJy}$

at  $870\ \mu\text{m}$  which is fainter than the two other extreme SMGs with  $S_{870,\text{intr}} > 10\text{mJy}$  ever found at  $z > 6$  (HFLS3 at  $z = 6.3$ ; Riechers et al. 2013, SPT0311-58 at  $z = 6.9$ ; Marrone et al. 2018) and is likely to be a member of a more common population of starburst galaxies at  $z = 6$ . Gravitational lensing magnifies the solid angles of background sources, enabling us to observe distant objects with increased spatial resolution.

In this paper, we report, with help of gravitational lensing magnification, the spatially-resolved detection of the CO(12-11) line and kinematic properties of the [O III]  $88\ \mu\text{m}$  and [N II]  $205\ \mu\text{m}$  lines in G09-83808. Throughout the paper, we adopt a cosmology with  $H_0 = 67.7\text{km s}^{-1}\text{Mpc}^{-1}$ ,  $\Omega_{\text{m}} = 0.3106$ , and  $\Omega_{\Lambda} = 0.6894$  (Planck Collaboration et al. 2020).

## 2 Observations and imaging

Paper I reported the initial results from ALMA Band-5 ([N II]  $205\ \mu\text{m}$  and 1.5-mm continuum) and Band-8 ([O III]  $88\ \mu\text{m}$  and 0.6-mm continuum) observations of G09-83808. The beam sizes were  $0''.84 \times 0''.77$  for the [N II]  $205\ \mu\text{m}$  line and  $0''.76 \times 0''.64$  for the [O III]  $88\ \mu\text{m}$  line. CO(12-11) line ( $\nu_{\text{rest}} = 1381.9951\text{GHz}$ ) is simultaneously observed with the [N II]  $205\ \mu\text{m}$  line in the ALMA Band-5 observations. The details of the observations are presented in Paper I.

By applying a clean mask constructed for 1.5 mm continuum (white solid line in the data panel of figure 1; see Paper I for details), we make channel maps of the CO(12-11) line at  $100\text{km s}^{-1}$  spectral resolution with a Briggs weighting of robustness parameter of 2.0, resulting in a beam size of  $0''.87 \times 0''.77$  (figure 9 in appendix 1).

The CO(12-11) line is integrated over a velocity range of  $-250\text{km s}^{-1}$  to  $+250\text{km s}^{-1}$ . The velocity offset is calculated relative to the systemic redshift of  $z = 6.0244 \pm 0.0003$  (see section 3.2). We resolve the lensed arcs of CO(12-11) emission in the integrated intensity map, where the peak line fluxes and noise levels are  $0.19 \pm 0.02\text{Jy beam}^{-1}\text{km s}^{-1}$  ( $7.8\sigma$ ) and  $0.15 \pm 0.02\text{Jy beam}^{-1}\text{km s}^{-1}$  ( $6.0\sigma$ ) in the north-west and south-east arcs, respectively (the cleaned image panel of figure 1). We also show the channel maps of [O III]  $88\ \mu\text{m}$  and [N II]  $205\ \mu\text{m}$  emissions with peak signal-to-noise ratio (SNR) of larger than 4 in the cleaned image panels of figure 2, 3. The noise level is  $1\sigma = 0.45\text{mJy/beam}$  per  $100\text{km s}^{-1}$  in the [O III]  $88\ \mu\text{m}$  cube,  $1\sigma = 0.13\text{mJy/beam}$  per  $100\text{km s}^{-1}$  in the [N II]  $205\ \mu\text{m}$  cube.

### 3 Lens modeling

We use the open-source code **GLAFIC** (Oguri 2010) to quantify the gravitational lensing effect and to reconstruct the source spatial structure with a parametric approach in the cleaned image plane. We assume that the mass distribution of the foreground lens galaxy, which is situated at  $z=0.776$  (Fudamoto et al. 2017), follows a singular isothermal ellipsoid with external shear and that the brightness distribution of the background source galaxy at  $z=6.02$  has a Sérsic profile. We first determine the lens parameters by modeling the 1.5-mm continuum map, which has the highest SNR among our ALMA data. We perform all lens modeling in the clean mask region (white solid line in the cleaned image panel of figure 1, 2, 3) to focus on the emitting region and reduce the amount of calculation. Then, we reconstruct the background source, where all parameters of the foreground source are fixed. The details of the method for determining the lens parameters and for the source reconstructions in the continuum maps and integrated intensity maps of the [O III] 88  $\mu\text{m}$  and the [N II] 205  $\mu\text{m}$  lines are described in Paper I. In this paper, we focus on source reconstruction in the integrated intensity map of the CO(12-11) line and the channel maps of the [O III] 88  $\mu\text{m}$  and [N II] 205  $\mu\text{m}$  lines.

#### 3.1 Integrated intensity map of the CO(12-11) emission

Since the SNR and angular resolution of the integrated intensity map of the CO(12-11) emission are worse than those of the 1.5-mm continuum map ( $75\sigma$  detection and  $0''.48 \times 0''.41$ ), it is not straightforward to determine all the parameters of the background source (spatial position  $(x, y)$ , total flux  $Sdv$ , effective radius  $R_e$ , major-to-minor axis ratio  $q$ , position angle  $\theta_q$ , and Sérsic index  $n$ ). Thus, we made some assumptions in our modeling. Given that the surface brightness profile of 1.5-mm continuum emission is well approximated by Sérsic profile of  $n=1.06\text{--}1.30$  (Paper I), we adopt an exponential disk profile with  $n=1$ . We fix the axis ratio and position angle to  $q=0.93$  and  $\theta_q=108$  deg, respectively, the values of which are derived from the 1.5-mm continuum data. Then, we fit the integrated intensity map of the CO(12-11) emission with the remaining free parameters of  $xy$ -position,  $Sdv$ , and  $R_e$ .

Figure 1 shows the cleaned image, obtained best-fit model image, residual, and reconstructed source model of CO(12-11) integrated intensity map. In the source panel, we also show the source models of the 1.5-mm continuum and integrated intensity map of [O III] 88  $\mu\text{m}$  line and [N II] 205  $\mu\text{m}$  line reconstructed in the same manner. To estimate the uncertainties of the derived source param-

eters, we add a  $1\sigma$  noise map convolved with a dirty beam to the clean image and fit the noise-added images. Then, we take the 16th and the 84th percentile of the best-fit values from 500 Monte Carlo runs as the uncertainties.

The intrinsic effective radius of the CO(12-11) emission is determined to be  $R_e = 0.08^{+0.05}_{-0.03}$  arcsec, corresponding to  $0.49^{+0.29}_{-0.19}$  kpc at  $z=6.02$ , after correction of the lensing effect. This value is consistent with the effective radius of the dust continuum emission ( $0''.11\text{--}0''.12$ ; Paper I), but is by a factor of two smaller than those of [O III] 88  $\mu\text{m}$  and [N II] 205  $\mu\text{m}$  emissions ( $0''.20\text{--}0''.21$ ; Paper I). The total magnification factor, given by the ratio between the total flux densities in the image and source plane, is calculated to be  $\mu_{\text{CO}(12-11)} = 9.3^{+7.2}_{-1.7}$ , which is consistent with those of the dust continuum at 0.6 mm and 1.5 mm, [O III] 88  $\mu\text{m}$ , and [N II] 205  $\mu\text{m}$  (8.0–8.4; Paper I). The position of CO(12-11) emission is consistent with that of the dust continuum, [N II] 205  $\mu\text{m}$ , and [O III] 88  $\mu\text{m}$  within the  $1\sigma$  uncertainty. In appendix 2, we provide a more detailed discussion of CO(12-11) size measurement.

According to past high-resolution observations of other high- $z$  SMGs, the CO emission region is smaller for a higher excitation level (e.g., Weiß et al. 2005; Apostolovski et al. 2019; Jarugula et al. 2021). In addition, it is known in high- $z$  SMGs that the low- $J$  CO emission region is more extended than that of dust and that the distribution of the mid/high- $J$  emission is similar to, or slightly more extended than, that of dust even at  $J_{\text{up}}=8,9$  (e.g., Spilker et al. 2015; Chen et al. 2017; Calistro Rivera et al. 2018; Apostolovski et al. 2019; Dong et al. 2019; Rybak et al. 2020; Jarugula et al. 2021). To our best knowledge, the CO(12-11) emission in G09-83808 is the most excited among the spatially-resolved CO rotational lines.

#### 3.2 Channel maps of the [O III] 88 $\mu\text{m}$ and [N II] 205 $\mu\text{m}$ emission

Both doubly-ionized oxygen and ionized nitrogen have higher ionization potentials than that of neutral hydrogen and work as tracers of ionized gas. The observed SNRs of the [O III] 88  $\mu\text{m}$  and [N II] 205  $\mu\text{m}$  channel maps with a channel width of  $100 \text{ km s}^{-1}$  are marginally higher than those of the CO(12-11) channel maps, and we extract kinematic information of the ionized gas through source reconstruction of the [O III] 88  $\mu\text{m}$  and [N II] 205  $\mu\text{m}$  channel maps, as follows. We adopt a circular Gaussian source with Sérsic index  $n=0.5$  rather than  $n=1$  as used in the modeling of the integrated intensity maps so that the fitting is more sensitive to the peak position. Since the angular resolution and SNRs are relatively low, a point source may fit better than an extended circular Gaussian

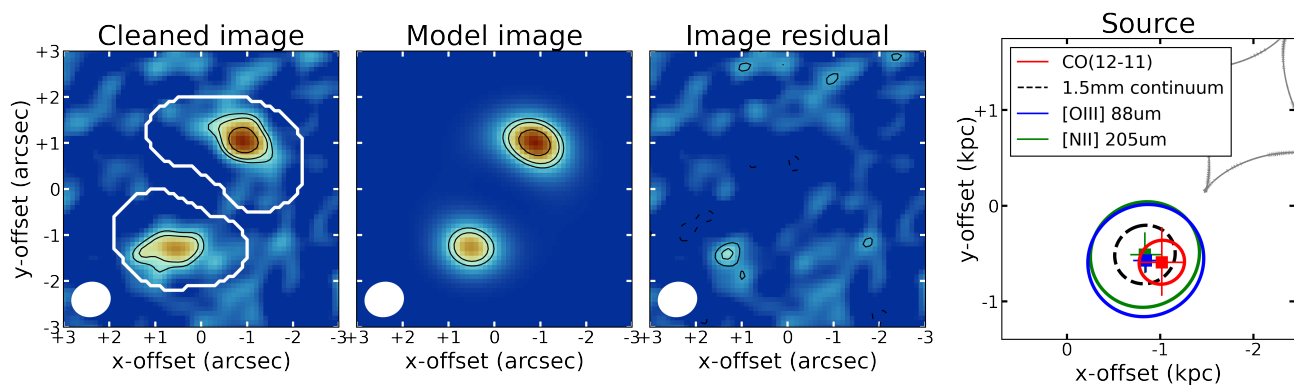


**Fig. 1.** Source reconstruction for the CO(12-11) integrated intensity map. Panels, from left to right, show the observed data (cleaned image), obtained best-fit model image, residuals, and reconstructed source model of CO(12-11). The black contours in the cleaned image and model image panel are drawn at  $[3, 4, 6, 8] \times \sigma$ , where  $\sigma = 0.02 \text{ Jy beam}^{-1} \text{ km s}^{-1}$ . Black contours in the residual panel are drawn at  $[-3, -2, 2, 3] \times \sigma$ . In the right-most panel, the reconstructed sources of the other emissions are also shown for comparison. The white solid line in the data panel indicates the mask region (the same as the clean mask) where the lens modeling is performed. The synthesized beam size is displayed in the lower-left corner of each panel. The filled squares and encircling ellipses in the rightmost panel indicate the positions and sizes of the sources. The gray solid line represents the caustics of our lens model.

source. Thus, we also perform the source reconstruction using a point source instead of a Gaussian source and adopt a better model based on their chi-square values. As a result, the point source model is adopted only for the  $-200 \text{ km s}^{-1}$  channel of [N II]  $205 \mu\text{m}$ . The uncertainties of the parameters are estimated in the same manner as described in section 3.1. Figure 2, 3 show the cleaned images, obtained best-fit model images, residuals, and source images of each channel map. The residual maps demonstrate that the fitting with a circular Gaussian source has generally worked well, remaining  $\lesssim 3\sigma$  peak residual. However, as shown in  $100 \text{ km s}^{-1}$  (1 source) row panels in figure 2, a non-negligible structure with  $\text{SNR} > 5$  remains at the  $100 \text{ km s}^{-1}$  channel of [O III]  $88 \mu\text{m}$  residual map using a single Gaussian source. Then, fitting using two circular Gaussian sources is performed ( $100 \text{ km s}^{-1}$  (2 sources) row panels). The **a** and **b** sources correspond to (**a1**, **a2**) and (**b1**, **b2**) components in the image plane and reduce the residuals to  $< 3\sigma$ . The best fit magnification factors of each [O III]  $88 \mu\text{m}$  source at  $-200 \text{ km s}^{-1}$ ,  $-100 \text{ km s}^{-1}$ ,  $0 \text{ km s}^{-1}$ ,  $100 \text{ km s}^{-1}$  (source a),  $100 \text{ km s}^{-1}$  (source b),  $200 \text{ km s}^{-1}$ , and  $300 \text{ km s}^{-1}$  are  $5_{-1}^{+1}$ ,  $4.7_{-0.8}^{+1.3}$ ,  $6.4_{-0.6}^{+2.2}$ ,  $6.5_{-0.4}^{+1.8}$ ,  $11.6_{-3.3}^{+1.6}$ ,  $14.1_{-1.4}^{+2.4}$ , and  $41_{-7}^{+9}$ , respectively. The best fit magnification factors of each [N II]  $205 \mu\text{m}$  source from  $-200 \text{ km s}^{-1}$  to  $200 \text{ km s}^{-1}$  are  $5.8_{-1.2}^{+2.5}$ ,  $5.0_{-1.3}^{+2.7}$ ,  $7_{-3}^{+6}$ ,  $10_{-2}^{+6}$ ,  $15_{-7}^{+8}$ , respectively. Line profiles of the observed clean images measured within the masked region and the reconstructed [O III]  $88 \mu\text{m}$  and [N II]  $205 \mu\text{m}$  sources are shown in figure 4. The redshifted parts of both emissions are closer to the caustics and more magnified than the blueshifted parts. The differential magnification causes the lensed image profiles to contain more flux at positive velocities, even though the intrinsic line profiles are more symmetrical.

Based on the single gaussian fit to the reconstructed profile of the [O III]  $88 \mu\text{m}$  line, the redshift is determined to be  $z = 6.0244 \pm 0.0003$ , about  $-100 \text{ km s}^{-1}$  shift from the previous value ( $z = 6.0269 \pm 0.0006$ ; Zavala et al. 2018).

#### 4 Physical properties of highly excited gas

The detection of CO(12-11) line (whose upper energy level is  $E_{\text{up}} = 431 \text{ K}$ ) suggests the existence of highly excited molecular gas. In order to investigate quantitatively the physical properties of the molecular gas, we model the CO SLED, using the 1D non-local thermal equilibrium (non-LTE) radiative transfer code RADEX (van der Tak et al. 2007). In the modeling, we incorporate, in addition to the CO(12-11) line detected in this work, the CO(2-1) (Zavala et al. in prep), CO(5-4), and CO(6-5) (Fudamoto et al. 2017; Zavala et al. 2018) lines detected in G09-83808 (Table 1). We use the galaxy-integrated flux densities for any of the lines for fair comparison even though the CO(2-1) and CO(12-11) line distributions were spatially resolved. In other words, the present analysis does not take into account the dependency of the gravitational lensing effect on the source position. Although the differential magnification effect could in principle affect the physical properties derived from a spatially unresolved CO SLED (e.g., Dong et al. 2019; Yang et al. 2019), we consider that its effect is negligible in the present analysis for the following reasons. First, with our lens model, the total magnification factors of the spatially extended [O III]  $88 \mu\text{m}$  and [N II]  $205 \mu\text{m}$  lines are consistent with those of compact dust continuum and CO(12-11) line (section 3.1). Therefore, the difference in the total magnification effect between the extended low- $J$  CO emission and compact high- $J$  CO emission is ex-

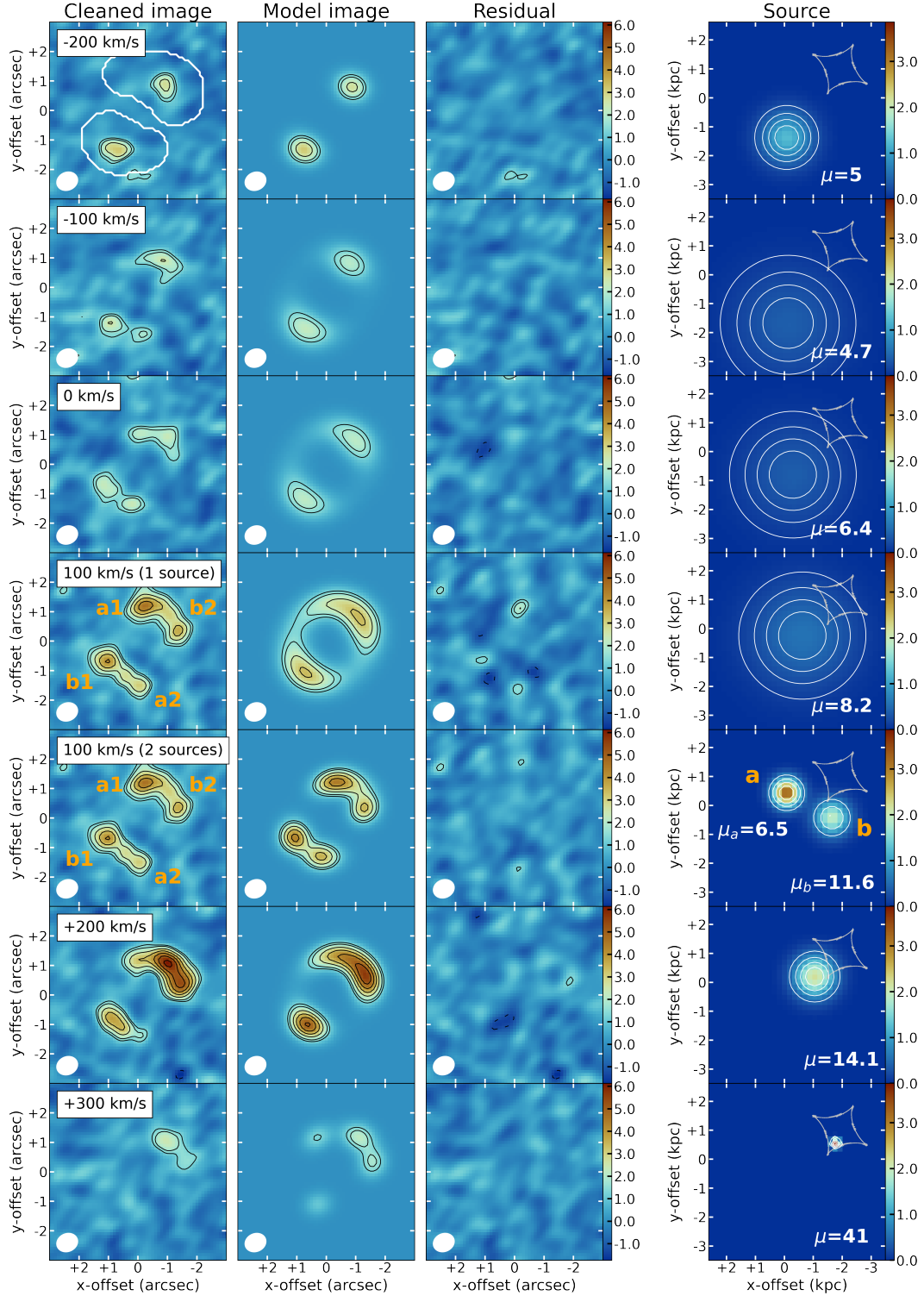


**Fig. 2.** Source reconstructions for the  $[\text{O III}] 88 \mu\text{m}$  channel maps. The peak SNRs of the cleaned  $[\text{O III}] 88 \mu\text{m}$  images are  $[7.8\sigma, 6.2\sigma, 5.6\sigma, 11.5\sigma, 14.6\sigma, 6.0\sigma]$ . White solid lines on the top-left panel show the mask region (clean mask) in which the lens modeling is performed. The black contours in the cleaned image panel and model image panel are drawn at  $[3, 4, 6, 8, 10, 12, 14] \times \sigma$ . The black dashed and solid contours in the residual panel are drawn at  $[-3, 3, 4, 5] \times \sigma$ . The white contours in the source panel show 20%, 40%, 60%, and 80% of the peak. The modeling at  $0 \text{ km s}^{-1}$  does not fit well with a single Sérsic source, leaving a residual of more than  $5\sigma$  (see  $100 \text{ km s}^{-1}$  (1 source) row), while the modeling with two Sérsic sources fit well with  $\sim 3\sigma$  residual ( $100 \text{ km s}^{-1}$  (2 sources) row). The (a1, a2) and (b1, b2) component in the image plane corresponds to a and b source in the source plane. The gray solid diamond-shaped lines in the source panel represent the caustics of our lens model. Colorbar units are  $\text{mJy beam}^{-1}$ . The magnification factor  $\mu$  of each channel is shown in the source panel. The synthesized beam size is displayed in the lower-left corner of each panel.

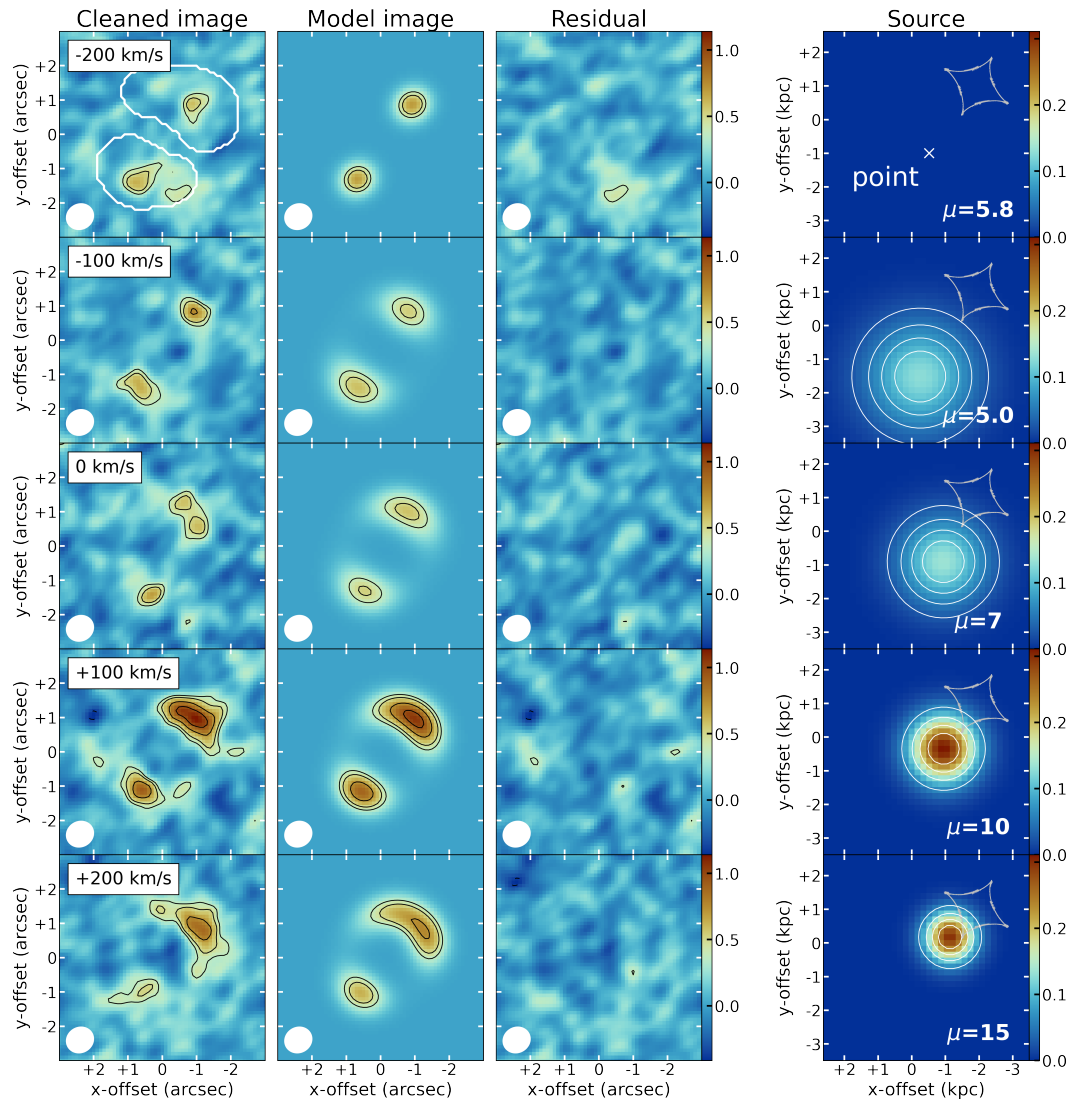


**Fig. 3.** Source reconstructions for the [N II] 205  $\mu\text{m}$  channel maps. The peak SNRs of the observed data are [4.9 $\sigma$ , 5.9 $\sigma$ , 5.3 $\sigma$ , 8.8 $\sigma$ , 7 $\sigma$ , 4 $\sigma$ ]. The contour levels and annotations are the same as figure 2. The modeling at  $-200 \text{ km s}^{-1}$  is performed with a point source whose position is shown as a white cross mark in the source panel.

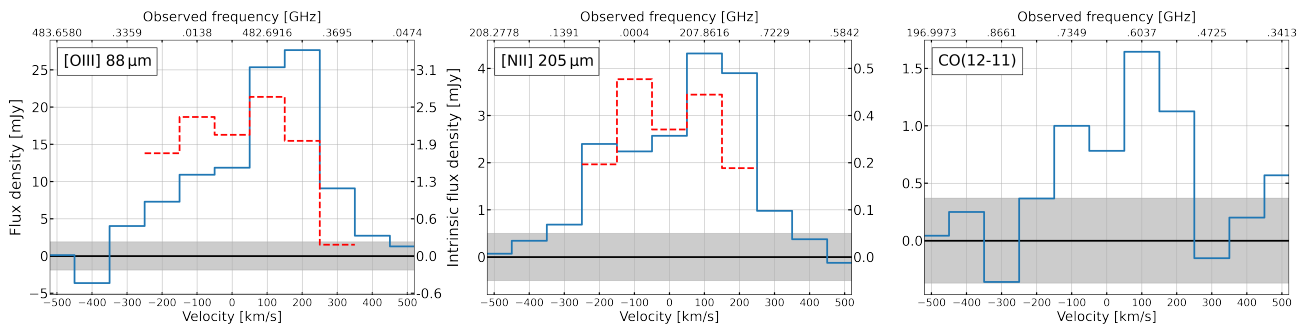


**Fig. 4.** Integrated line spectra for [O III] 88  $\mu\text{m}$ , [N II] 205  $\mu\text{m}$ , and CO(12-11), measured within the masked region in the cleaned images (blue solid lines) and their reconstructed sources (red dashed lines). The intrinsic flux density is plotted on the right axis. To make it easier to compare the profiles, source plane line profiles are multiplied by the total magnifications. Gray shaded areas represent the  $\pm 1\sigma$  uncertainties.



pected to be small. Secondly, as shown in figure 5, the line profiles of CO(2-1), CO(5-4), CO(6-5), and CO(12-11) do not differ significantly. And the total magnification factors of [O III]  $88 \mu\text{m}$  and [N II]  $205 \mu\text{m}$  emissions which are obtained by the source reconstructions for each channel map are  $8.4 \pm 1.1$  and  $8 \pm 3$ , respectively, which are consistent with the average magnification factors of  $8.09^{+0.08}_{-0.08}$  and  $8.3^{+0.1}_{-0.2}$  derived from the source reconstructions for the integrated intensity maps. Therefore, the difference in the magnification effect due to the differences in velocity structure is also expected not to be significant.

The inputs to RADEX are a kinetic temperature ( $T_{\text{kin}}$ ), molecular hydrogen density ( $n_{\text{H}_2}$ ), and CO column density ( $N_{\text{CO}}$ ). We assume an expanding sphere geometry and set  $dV = 400 \text{ km s}^{-1}$ , which is roughly the FWHM of the CO lines, the background temperature to 19.2 K, and the cosmic microwave background temperature to  $z = 6.02$ . We search for the minimum chi-square within the parameter space of  $T_{\text{kin}} = 20 - 700 \text{ K}$ ,  $\log(n_{\text{H}_2}/\text{cm}^{-3}) = 2 - 6.7$ ,  $\log(N_{\text{CO}}/\text{cm}^{-2}) = 16 - 20.5$ . Our fitting attempt with the CO SLED with a single component results in a solution that does not converge within the search range. Hence, the model requires an additional component. In our case of G09-83808, the number of the observed CO line data is only four; thus, some additional constraints on the free parameters are necessary to perform two-component model-fitting and obtain meaningful results. A constraint that we set is that the molecular gas mass must not exceed the dynamical mass ( $M_{\text{dyn}} = 5 \times 10^{10} M_{\odot}$  including  $1\sigma$  error; Zavala et al. 2018). Another constraint is that the CO SLED of both the warm and cool gas components satisfy  $L_{\text{CO}(13-12)} < L_{\text{CO}(12-11)}$ . We also assume that the temperature of the cold component is  $T_{\text{kin,cold}} < 100 \text{ K}$ . In fact, most of the local ULIRGs, high- $z$  quasars, and SMGs satisfy the second and third constraints (e.g., Mashian et al. 2015; Li et al. 2020; Yang et al. 2017). We note that the determined  $T_{\text{kin}}$  or  $n_{\text{H}_2}$  would go beyond the search ranges without these constraints in the model fitting. We add a  $1\sigma$  Gaussian noise to the observed CO data and fit the noise-added CO SLED. This process is repeated 200 times to obtain the mean values and standard deviations.

The results are  $T_{\text{kin}} = 55 \pm 16 \text{ K}$ ,  $\log(n_{\text{H}_2}/\text{cm}^{-3}) = 3.5 \pm 0.5$  for the cold component and  $T_{\text{kin}} = 320 \pm 170 \text{ K}$ ,  $\log(n_{\text{H}_2}/\text{cm}^{-3}) = 5.4 \pm 0.6$  for the warm component. The temperature of the cold component is consistent with that of the dust estimated from dust spectral energy distribution modeling (51 K; Paper I). The results show that more than 99% of the CO(12-11) emission originates from the warm component (figure 6). This implies that the warm and dense molecular gas is concentrated in the center of this galaxy ( $R_e = 0.49^{+0.29}_{-0.19} \text{ kpc}$ ).

**Table 1.** CO line data (not corrected for lens amplification)

Line	$S\Delta V$ ( $\text{Jy km s}^{-1}$ )	$L$ ( $10^8 L_{\odot}$ )	References*
CO(2-1)	$0.6 \pm 0.1$	$0.7 \pm 0.1$	(1)
CO(5-4)	$1.6 \pm 0.3$	$4.8 \pm 0.9$	(2)
	$0.9 \pm 0.3$	$2.8 \pm 0.9$	(3)
CO(6-5)	$0.9 \pm 0.3$	$3 \pm 1$	(2)
	$0.9 \pm 0.2$	$3.1 \pm 0.9$	(3)
CO(12-11)	$0.49 \pm 0.09$	$3.5 \pm 0.7$	This work

\* (1) Zavala et al. 2022, (2) Zavala et al. 2018, (3) Fudamoto et al. 2017.

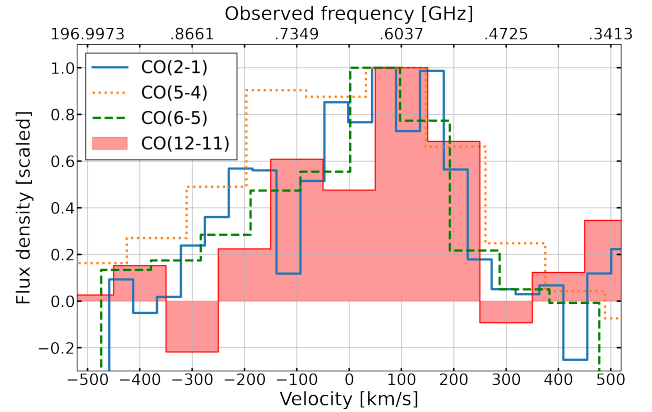


**Fig. 5.** The CO(12-11) line profile measured in the cleaned image compared with those of CO(2-1) from Zavala et al. (2022), CO(5-4), and CO(6-5) from Zavala et al. (2018). The lines are scaled to match the line peak to compare the line profiles.

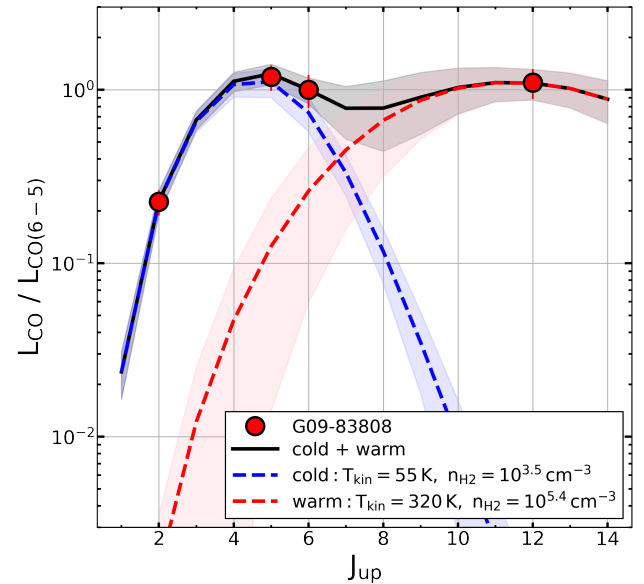


**Fig. 6.** CO SLED from two-component fitting. The observed data are shown with red points with error bars. The contributions from the cold and warm components are shown with blue and red dashed lines, respectively. The total best-fit model is shown with a black line. Color-shaded regions represent the  $1\sigma$  uncertainties.



Finally, we discuss the potential effect of dust attenuation, which we have not considered in the analysis. In general, the observed line intensities are affected by dust extinction in the form:  $I = I_0 (1 - e^{-\tau_\nu}) / \tau_\nu$ , where  $\tau_\nu = (\nu/\nu_0)^\beta$  (e.g., Rangwala et al. 2011). Here, the dust optical depth is unity at  $\nu = \nu_0 (= c/\lambda_0)$  and  $\beta$  is the emissivity index. Adopting  $\lambda_0 = 150 \mu\text{m}$  and  $\beta = 2.5$  (Paper I), we find that the effect of dust attenuation on the CO(12-11) line at the rest-frame wavelength of  $\sim 200 \mu\text{m}$  is roughly 20%. If the dust extinction is stronger than expected, the intrinsic brightness of CO(12-11) will be greater, i.e., the temperature of the warm gas will be even higher than the estimated above.

## 5 Discussion and conclusion

### 5.1 Kinematics of ionized gas

Observationally, it remains unclear what causes extreme starburst in the central compact regions of SMGs, i.e., how the gas is transported to the central compact regions. One possible mechanism is a gas-rich major merger, which is known from observations and simulations to lead the transportation (e.g., Mihos & Hernquist 1996; Tacconi et al. 2008). Another is a so-called cold stream or minor merger process. In this scenario, starburst is caused by the migration into the center of giant star-forming clumps produced by gravitational instability and fragmentation in semi-continuously fed, gas-rich disks (e.g., Noguchi 1999; Dekel et al. 2009a, 2009b; Genzel et al. 2011; Tadaki et al. 2020). In any case, the induced central starburst would build a central bulge component characteristic of compact quiescent galaxies, which are likely to be the post-evolutionary form of SMGs.

The positions and effective radii of the reconstructed sources in each [O III]  $88 \mu\text{m}$  and [N II]  $205 \mu\text{m}$  channel are summarized in figure 7. An almost monotonic velocity gradient is found over  $\sim 2 \text{ kpc}$  centered at the compact dust continuum regions ( $R_e \sim 0.64 \text{ kpc}$ ; Paper I) in both [O III]  $88 \mu\text{m}$  and [N II]  $205 \mu\text{m}$  line maps. And, the reconstructed line profiles of [O III]  $88 \mu\text{m}$  and [N II]  $205 \mu\text{m}$  have double-horn shapes as shown in figure 4. These results could be interpreted as a signature of a rotating disk, but it is difficult to reject the other possibilities such as mergers and outflows with the current data alone due to the limited angular resolution and SNR (e.g., Simons et al. 2019; Rizzo et al. 2022).

Figure 7 also shows the two reconstructed sources, designated as sources **a** and **b**, where we employ two Sérsic sources, at  $100 \text{ km s}^{-1}$  in the [O III]  $88 \mu\text{m}$  source map. Sources **a** and **b** are located along the direction perpen-

dicular to the major axis of disk rotation. These components are not detected in the 0.6 mm, 1.5 mm continuum map and [N II]  $205 \mu\text{m}$  map. Paper I reported that the 0.6 mm, 1.5 mm continuum map and integrated intensity map of [N II]  $205 \mu\text{m}$  in G09-83808 is well modeled by a single exponential disk source model, whereas for the integrated intensity map of [O III]  $88 \mu\text{m}$ , some residuals remain in the edges of the two arcs just like in the modeling of [O III]  $88 \mu\text{m}$   $100 \text{ km s}^{-1}$  channel map with a single Gaussian source ( $100 \text{ km s}^{-1}$  (1 source) row panels in figure 2). Given these facts, these two sources seem to deviate from the primary disk, so we here refer to them as 'sub-components'.

The **a** and **b** sub-components account for  $13 \pm 2\%$  and  $12 \pm 2\%$  of the total [O III]  $88 \mu\text{m}$  luminosity, respectively. From the non-detection ( $< 3\sigma$ ) of the sub-components in the dust continuum, the lower limits of the  $L_{[\text{O III}]} / L_{\text{IR}}$  ratios are derived to be  $6.4 \times 10^{-3}$  and  $4.9 \times 10^{-3}$  for sub-components **a** and **b**, respectively, under the assumption of the same SED as in Paper I. Oxygen is doubly excited only by hard radiation from the hottest stars (or AGN). Paper I showed that the  $L_{[\text{O III}]} / L_{\text{IR}}$  ratio is very sensitive to a variation in the age of star formation, which alters the energy distribution of incident radiation from the photoionization model. The derived high ratio of  $L_{[\text{O III}]} / L_{\text{IR}}$  indicates that star formation is going on in these sub-components (see figure 3 of Paper I). In fact, the high ratio is consistent with those of local dwarf galaxies ( $10^{-3} - 10^{-2}$ ; Cormier et al. 2015). In massive star-forming galaxies at  $z=2-4$ , kpc-scale clumps are gravitationally bounded and are considered to form bulges through some internal process in extended rotating disks (e.g., Genzel et al. 2011; Tadaki et al. 2017). Also, the presence of star-forming clumps can be explained in the major merger scenario (e.g., Calabrò et al. 2019). It is difficult to determine from the current data alone whether the [O III]  $88 \mu\text{m}$  sub-components are gravitationally bound clumps or have an external origin, such as clumpy gas accretion.

Future observations of bright emissions such as [C II]  $158 \mu\text{m}$  line with a higher angular resolution will enable us to quantitatively investigate the kinematics of the multiple phases of the ISM and nature of the sub-components.

### 5.2 Heating source of CO(12-11) emission

Detection of high- $J$  CO lines suggests the existence of high-energy heating sources. The CO lines from  $J_{\text{up}} = 5$  to  $J_{\text{up}} = 13$  in the nearest AGN, Mrk 231, were studied with Herschel observations (van der Werf et al. 2010). They argued that the measured CO( $J > 10$ ) luminosities

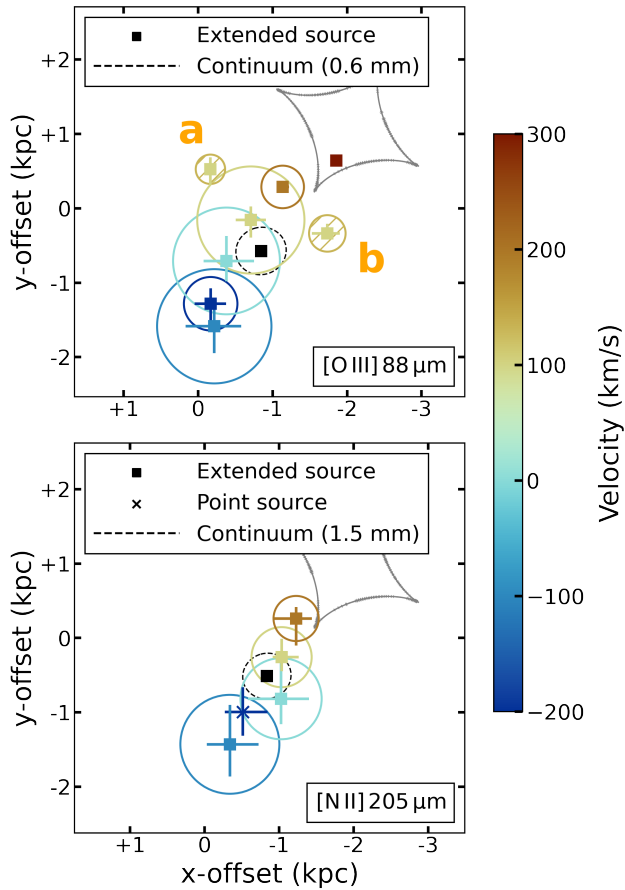


**Fig. 7.** Plot of the reconstructed source positions on the (upper panel) [O III]  $88 \mu\text{m}$  and (lower) [N II]  $205 \mu\text{m}$  channel maps. Filled squares and crosses indicate the positions of the extended and point sources, respectively. Circles represent the effective radii. The reconstructed  $0.6 \text{ mm}$  and  $1.5 \text{ mm}$  continuum sources are marked with black squares and dashed ellipses. Two hatched components (**a** and **b**) at [O III]  $88 \mu\text{m}$   $0 \text{ km s}^{-1}$ , located along the minor axis of the rotation disk, are the reconstructed sources with two Sérsic source models. The caustics of our lens model are shown in gray solid lines.

could not be explained with dense photodissociation-region models and that X-rays from the accreting supermassive black hole (SMBH) dominantly caused the excitation of the  $\text{CO}(J > 10)$  emission. Furthermore,  $\text{CO}(J > 10)$  emission has been detected in quasars at  $z = 6 - 7$  (Gallerani et al. 2014; Wang et al. 2019; Li et al. 2020) and is considered to be radiated from X-ray-dominated regions around AGNs. Figure 8 shows  $\text{CO}(6-5)$ -normalized CO SLEDs of G09-83808, local starburst galaxies, local AGNs (Mashian et al. 2015; Rosenberg et al. 2015), and average of 4 quasars at  $6 < z < 7$  (Carniani et al. 2019; Li et al. 2020). The high ratio of  $L_{\text{CO}(12-11)}/L_{\text{CO}(6-5)} = 1.1 \pm 0.2$  in G09-83808 agrees better with those in local AGNs and  $6 < z < 7$  quasars than those in local starburst galaxies. This comparison suggests that G09-83808 hosts a dust-obscured AGN in the center although we cannot exclude other possibilities,

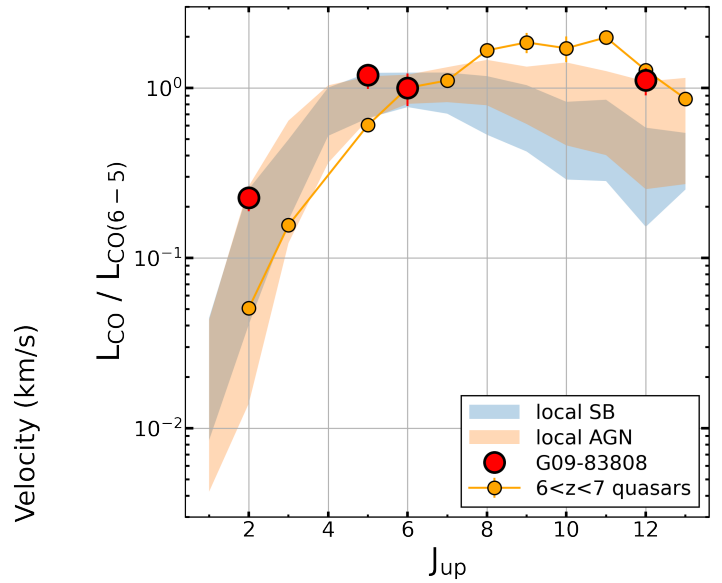


**Fig. 8.**  $\text{CO}(6-5)$  normalized CO SLED of G09-83808 and other systems (local starburst galaxies, local AGNs, and  $6 < z < 7$  quasars) for comparison. The data points of the local starburst galaxies and local AGNs are shown with shaded regions in sky-blue and orange, respectively (Rosenberg et al. 2015; Mashian et al. 2015). That of the  $6 < z < 7$  quasars is also shown in orange (Carniani et al. 2019; Li et al. 2020).

such as shock (e.g., Meijerink et al. 2013; Saito et al. 2017) and extreme starburst (e.g., Riechers et al. 2013), with the current data alone. One powerful tool to explore the dust-obscured AGNs is polycyclic aromatic hydrocarbon emission features in the rest-frame mid-infrared spectrum because small PAHs would be destroyed by hard X-rays from AGN (e.g., Moorwood 1986; Imanishi & Dudley 2000). Mid Infrared Instrument on *James Webb Space Telescope* will enable us to observe these lines. Exploration of dust-obscured AGNs will help us reveal the nature of the early co-evolution of SMBHs and host galaxies.

## Acknowledgments

We thank the referee for a number of constructive comments and suggestions that improved the paper. We wish to thank Masamune Oguri and Justin S. Spilker for lots of advice about gravitational lens modeling. This paper makes use of the following ALMA data: ADS/JAO.ALMA#2019.1.01307.S. ALMA is a partnership of ESO (representing its member states), NSF (USA) and NINS (Japan), together with NRC (Canada), MOST and ASIAA (Taiwan), and KASI (Republic of Korea), in cooperation with the Republic of Chile. The Joint ALMA Observatory is operated by ESO, AUI/NRAO and NAOJ. We thank the ALMA staff and in particular the EA-ARC staff for their support. This work was supported by JSPS KAKENHI Grant Numbers 20K14526 and 17H06130, and by the NAOJ ALMA Scientific Research Grant Number 2017-06B. Data analysis was in part carried out on the Multiwavelength

Data Analysis System operated by the Astronomy Data Center (ADC), National Astronomical Observatory of Japan (NAOJ).

## Appendix 1 CO(12-11) channel maps

Figure 9 shows the cleaned CO(12-11) channel maps with a robust parameter of 2.0. Due to the low SNR, we didn't perform the source reconstructions for each channel.

## Appendix 2 CO(12-11) intrinsic source size

In the section 3.1, the CO(12-11) intrinsic source size is derived to be  $R_e = 0.08^{+0.05}_{-0.03}$  arcsec with the help of lensing magnification ( $\mu_{\text{CO}(12-11)} = 9.3^{+7.2}_{-1.7}$ ). However, since the angular resolution is  $0''.87 \times 0''.77$ , the effective angular resolution in the source plane is  $0''.8/\sqrt{\mu} \sim 0''.26$ , corresponding to the disks with a radius of  $\sim 0''.13$ . This value is  $\sim 1.6$  times larger than the derived source size, so it seems strange that the source size is measured despite the lack of angular resolution. There are two possible explanations for the reason why GLAFIC can estimate a source size smaller than the beam size.

First, since the beam profile is known, in principle, the size of objects smaller than the beam size can be measured (if not too small).

Second, since we assume a source profile (Sérsic profile with an index of  $n = 1$ ) in this modeling, we do not necessarily need to directly resolve the object to measure its size. For example, if the profile is fixed, it would be possible to regulate the source size by extrapolating the source profile to the center using information from the fitting of the outskirt parts and the central flux, and this may be what is happening. In fact, the magnification map shown in figure 10, shows that the outskirt parts near the caustics are magnified as high as about 15-20 times, although the average magnification factor is  $\sim 9.3$ . Regarding the second point, fitting with the source profile free would provide more robust results. Therefore, we perform the fitting with the Sérsic index also free. Consequently, the obtained effective radius don't change significantly ( $R_e = 0.09^{+0.07}_{-0.04}$  arcsec,  $n = 0.6^{+3.3}_{-0.06}$ ).

In addition, we try the source reconstructions using clean images with different robust parameters of 1.5, 1.0, 0.5, 0.0, and  $-0.5$  (the same as that of dust emission). When imaging with robust parameters of 0.0 or less, the integrated flux density is less than  $5\sigma$ , so we don't perform the modeling. With the parameter of 0.5, the resolution is  $0''.66 \times 0''.59$  and the source size is  $R_e = 0.08^{+0.05}_{-0.03}$  arcsec, which is consistent with that of the parameter of 2.0.

Finally, we simulate the source size measurements by making mock images. Using GLAFIC code, we vary the

effective radius of the Sérsic source from  $0''.01$  to  $0''.14$  in  $0''.01$  increments while fixing the other parameters at the best-fit parameters obtained in section 3.1 to create the mock lensed images. We add the  $1\sigma$  noise map convolved with a dirty beam to the images and perform the source reconstructions for the noise-added mock images in the same manner as section 3.1. Then, we take the median values, 16th and the 84th percentile of the best-fit values from 500 Monte Carlo runs as the best-fit measured sizes and uncertainties, respectively. In figure 11, the measured effective radius ( $R_{\text{model}}$ ) is plotted as a function of the true effective radius ( $R_{\text{true}}$ ). This result implies that it is difficult to distinguish the extended source from the point source in the region of  $R_{\text{true}} \lesssim 0.04$  arcsec. However, when the  $R_{\text{model}} \sim 0.08$  arcsec, it is possible to measure the source size as the extended source.

From these results, we have concluded that the intrinsic source size of CO(12-11) emission is measured as an extended source, not a point source. Note that we used the measured size when the Sérsic index is fixed to 1.0, in order to make the size comparison with other emissions fairer.

## References

- Apostolovski, Y., et al. 2019, A&A, 628, A23  
 Calabrò, A., et al. 2019, A&A, 632, A98  
 Calistro Rivera, G., et al. 2018, ApJ, 863, 56  
 Carniani, S., et al. 2019, MNRAS, 489, 3939  
 Chen, C.-C., et al. 2017, ApJ, 846, 108  
 Cormier, D., et al. 2015, A&A, 578, A53  
 Dekel, A., Sari, R., & Ceverino, D. 2009a, ApJ, 703, 785  
 Dekel, A., et al. 2009b, Nature, 457, 451  
 Dong, C., et al. 2019, ApJ, 873, 50  
 Fudamoto, Y., et al. 2017, MNRAS, 472, 2028  
 Gallerani, S., Ferrara, A., Neri, R., & Maiolino, R. 2014, MNRAS, 445, 2848  
 Genzel, R., et al. 2011, ApJ, 733, 101  
 Glazebrook, K., et al. 2017, Nature, 544, 71  
 Imanishi, M., & Dudley, C. C. 2000, ApJ, 545, 701  
 Jarugula, S., et al. 2021, ApJ, 921, 97  
 Li, J., et al. 2020, ApJ, 889, 162  
 Marrone, D. P., et al. 2018, Nature, 553, 51  
 Mashian, N., et al. 2015, ApJ, 802, 81  
 Meijerink, R., et al. 2013, ApJL, 762, L16  
 Mihos, J. C., & Hernquist, L. 1996, ApJ, 464, 641  
 Moorwood, A. F. M. 1986, A&A, 166, 4  
 Noguchi, M. 1999, ApJ, 514, 77  
 Oguri, M. 2010, PASJ, 62, 1017  
 Planck Collaboration, et al. 2020, A&A, 641, A1  
 Rangwala, N., et al. 2011, ApJ, 743, 94  
 Riechers, D. A., et al. 2013, Nature, 496, 329  
 Rizzo, F., Kohandel, M., Pallottini, A., Zanella, A., Ferrara, A., Vallini, L., & Toft, S. 2022, arXiv e-prints, arXiv:2204.05325  
 Rosenberg, M. J. F., et al. 2015, ApJ, 801, 72

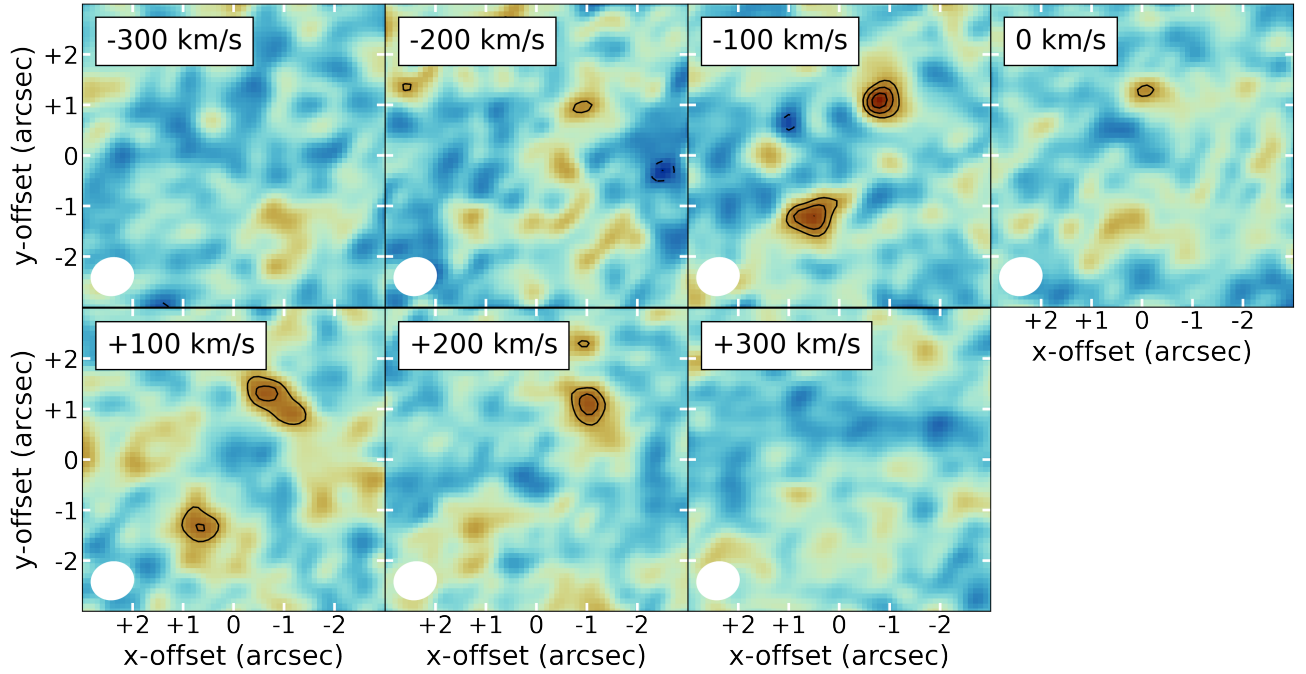


**Fig. 9.** Cleaned CO(12-11) channel maps from  $-300 \text{ km s}^{-1}$  to  $300 \text{ km s}^{-1}$  with robust parameter of 2.0. The peak SNRs are  $[2.7\sigma, 3.4\sigma, 5.7\sigma, 3.4\sigma, 4.4\sigma, 4.6\sigma, 2.5\sigma]$ . The black contours are drawn at  $[3, 4, 5] \times \sigma$  where  $1\sigma = 0.11 \text{ mJy beam}^{-1}$ . The synthesized beam size is displayed in the lower-left corner.

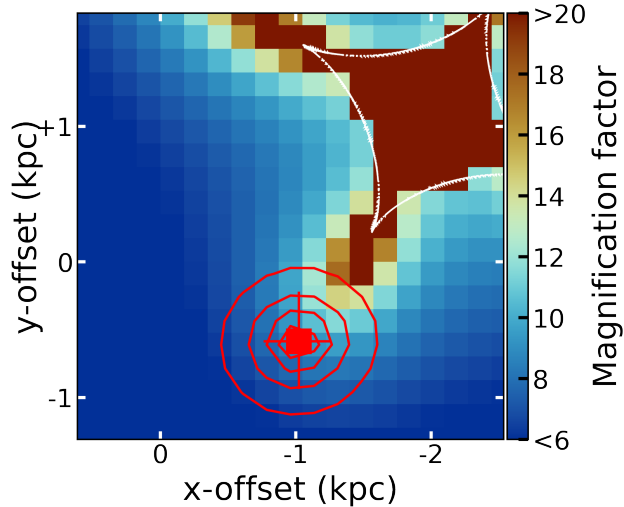


**Fig. 10.** Distribution of the magnification factor in the source plane at  $z = 6.0255$ . The red contours represent the 20%, 40%, 60%, 80% of the peak of the reconstructed CO(12-11) integrated intensity map. The filled red square and cross indicate the peak position and its uncertainty (see section 3.1). The caustics of our lens model is shown as the white solid line.

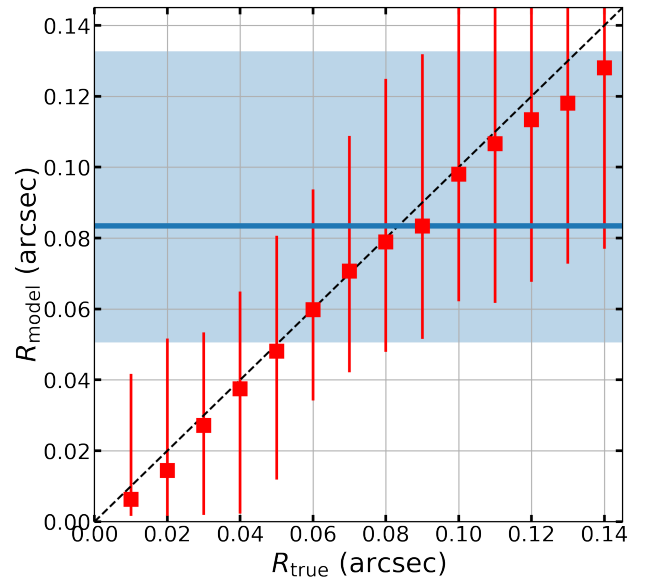


**Fig. 11.** Model vs. true effective radius for intrinsic CO(12-11) emission. The blue line and shaded region represent the estimated CO(12-11) intrinsic source size ( $R_e = 0.08^{+0.05}_{-0.03} \text{ arcsec}$ ). The red squared dots are the median values of measured effective radii with  $1\sigma$  uncertainties from 500 Monte Carlo runs. The black dashed line denotes the relation  $R_{\text{true}} = R_{\text{model}}$ .

Rybak, M., Hodge, J. A., Vegetti, S., van der Werf, P., Andreani, P., Graziani, L., & McKean, J. P. 2020, MNRAS, 494, 5542

Saito, T., et al. 2017, ApJ, 835, 174

Simons, R. C., et al. 2019, ApJ, 874, 59

Spilker, J. S., et al. 2015, ApJ, 811, 124

Tacconi, L. J., et al. 2008, ApJ, 680, 246

Tadaki, K., et al. 2017, ApJ, 834, 135

- 
- Tadaki, K., et al. 2020, *ApJ*, 889, 141  
Tadaki, K., et al. 2022, *PASJ*, 74, L9  
van der Tak, F. F. S., Black, J. H., Schöier, F. L., Jansen, D. J.,  
& van Dishoeck, E. F. 2007, *A&A*, 468, 627  
van der Werf, P. P., et al. 2010, *A&A*, 518, L42  
Wang, F., Wang, R., Fan, X., Wu, X.-B., Yang, J., Neri, R., &  
Yue, M. 2019, *ApJ*, 880, 2  
Weiß, A., Walter, F., & Scoville, N. Z. 2005, *A&A*, 438, 533  
Yang, C., et al. 2017, *A&A*, 608, A144  
Yang, C., et al. 2019, *A&A*, 624, A138  
Zavala, J. A., et al. 2018, *Nature Astronomy*, 2, 56  
Zavala, J. A., et al. 2022, *ApJ*, 933, 242